



Influence of geometry on the galloping instability of rectangular cylinders in the Reynolds number range 1,000–10,000

Mark A. Feero, Ahmed M. Naguib^{*}, Manoochehr M. Koochesfahani^{*}

Department of Mechanical Engineering, Michigan State University, East Lansing, MI, 48824, USA



ARTICLE INFO

Article history:

Received 10 July 2019

Received in revised form 13 November 2019

Accepted 14 January 2020

Available online 28 January 2020

ABSTRACT

Wind tunnel experiments were used to investigate the effects of geometry on the transverse galloping behavior of nominally rectangular cylinders at Reynolds numbers from 1,000 to 10,000. Static measurements of the lift and the drag forces were used to determine the variation of the normal force coefficient with angle-of-attack, in accordance with the typical quasi-steady description of galloping. Cylinders with unity chord-to-thickness ratio (side ratio) were found to vary from unstable, to neutrally stable, to stable as the corner radius was increased from sharp, to half-round, to fully-round, with this effect diminishing with decreasing Reynolds number. Cylinders with side ratios of 2 or 3 demonstrated either stability over the entire Reynolds number range, or a transition from unstable to stable with increasing Reynolds number, depending on corner radius. The results demonstrated that in general, increasing the corner radius had a stabilizing effect.

© 2020 Elsevier Ltd. All rights reserved.

1. Introduction

Elastically mounted cylinders with non-circular cross section are susceptible to a flow induced instability known as galloping due to the fact that the aerodynamic forces on the body change with its orientation to the oncoming flow. When a cylinder is elastically mounted in the transverse direction, i.e. the y -direction as defined in Fig. 1, an oscillation velocity \dot{y} in this direction will cause a change in the cylinder's effective angle-of-attack, α . Note that positive y is defined in the downward direction, as in convention in galloping literature. As such, oscillating lift and drag forces will occur. The normal force coefficient along the y -direction is related to the lift and drag coefficients, viz.:

$$C_y = \frac{F_y}{1/2\rho U_\infty^2 dl} = -\frac{1}{\cos \alpha^2} (C_L \cos \alpha + C_D \sin \alpha), \quad (1)$$

where $C_L = F_L/(1/2\rho U_{\text{rel}}^2 dl)$ and $C_D = F_D/(1/2\rho U_{\text{rel}}^2 dl)$ are the lift and the drag coefficients, respectively, U_∞ is the steady freestream velocity, U_{rel} is the instantaneous oncoming velocity relative to the cylinder, ρ is the fluid density, d is the cylinder width and l is the cylinder span. F_L and F_D are the lift and the drag forces, respectively, and F_y is the normal force. If the oscillation in F_y is such that it increases with α , this effectively produces negative fluid damping and the structure could become unstable; a phenomenon known as transverse galloping. That is, if $\partial C_y / \partial \alpha > 0$, the cylinder meets the necessary aerodynamic condition for galloping. Galloping is a phenomenon that can adversely affect structures

^{*} Corresponding authors.

E-mail addresses: naguib@egr.msu.edu (A.M. Naguib), koochesf@egr.msu.edu (M.M. Koochesfahani).

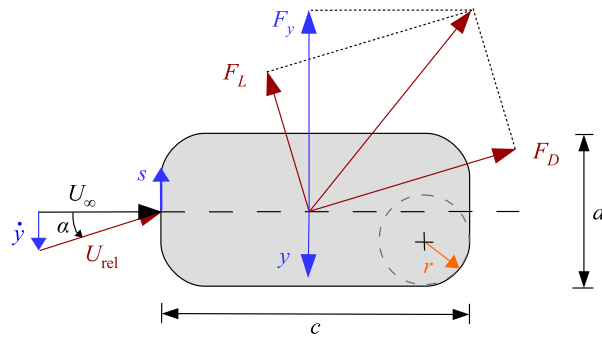


Fig. 1. Rectangular cylinder cross-section geometry and forces acting on the body when moving in the transverse direction at a velocity \dot{y} .

such as ice coated power lines, bridge decks and stalled wings by causing large amplitude oscillations that are divergent with increasing freestream velocity (Blevins, 2001; Naudascher and Rockwell, 2005). Another type of structure that may be susceptible to the galloping instability is the suspension line used in parachutes (Siefers et al., 2013), such as those used to attach the payload to the canopy in precision airdrop systems (Bergeron et al., 2009). The cross-section of these braided cables is not circular, but is more accurately described as a rectangle with a side ratio c/d (where c is chord length) in the range 2–3 and rounded corners (Siefers et al., 2013). Understanding the aerodynamic behavior relating to the transverse galloping of such nominally rectangular cylinders is therefore fundamental to the prediction and mitigation of this instability.

The analysis of galloping typically assumes that the forces acting on the body vary in a quasi-steady manner; that is, the lift and the drag forces depend only on the magnitude and direction of the instantaneous relative velocity, U_{rel} . However, this assumption is only valid when the time scale of oscillation is much longer than the time scale associated with vortex shedding in the wake of the body. The relevant time scale ratio is expressed non-dimensionally as the reduced velocity $U_r = U_\infty/(df)$, where f is the frequency of oscillation. Classically, it has been argued that quasi-steady analysis is valid for $U_r > 20$ (Blevins, 2001). In comparison, vortex shedding Strouhal numbers for rectangular cylinders are typically in the range 0.08–0.2, which corresponds to $U_r = 5 - 13$ (Mannini et al., 2014; Norberg, 1993). The quasi-steady approximation typically works well for structures with a high Scruton number (or the product of the mass and the damping ratios), which leads to a large value of the critical reduced velocity for the onset of galloping. For structures with low Scruton number, the critical velocity can be substantially lower such that it is comparable to that of vortex shedding. Under these conditions, vortex-induced and galloping oscillations interact, and the assumption of quasi-steadiness breaks down. A number of studies have considered these low Scruton number scenarios and the interaction between vortex shedding and galloping; e.g. Bearman et al. (1987) and Massai et al. (2018). It is also noteworthy that Bearman and Luo (1988) showed that the validity of the quasi-steady assumption should not only take into account the reduced velocity, but also the amplitude of oscillation. If the assumption of quasi-steady behavior is valid, then the results from static wind tunnel tests can be used to describe the variation of the aerodynamic forces with α .

The goal of the present study is to investigate the effects of geometry on the aerodynamic behavior of nominally rectangular cylinders with side ratio c/d and corner radius ratio r/d as it pertains to the transverse galloping instability. This is a fundamental investigation in the behavior of rectangular cylinders that are relevant to the application of parachute suspension lines. This work is motivated by recent experimental studies from Siefers et al. (2013, 2014) who showed that large amplitude oscillations were present on suspension lines at frequencies much lower than those of vortex shedding in the wake, and the authors suspected transverse galloping could be the cause. The Reynolds number range considered in this work is $Re_d = U_\infty d/\nu = 1000-10,000$, where ν is the kinematic viscosity, which is relevant to the suspension lines of precision airdrop systems. Over this relatively low Reynolds number range, there is limited information in the literature on the flow characteristics of rectangular cylinders, even for sharp-cornered cylinders. To the best of the authors knowledge, there have been no studies regarding the effect of corner radius on galloping for $c/d > 1$. In this work, static wind tunnel testing on geometries with $1 \leq c/d \leq 3$ and $0 \leq r/d \leq 0.5$ was performed to determine the variation in the lift and the drag forces, and surface-pressure distributions with angle-of-attack on rigidly mounted models. The variation in C_y with α was computed from C_L and C_D , and from this the $\partial C_y/\partial \alpha$ galloping criterion was assessed. Surface pressure measurements were also performed to gain additional insight into the cause of observed $C_y(\alpha)$ trends. The bulk of the results in this work were originally presented in a conference paper (Feero et al., 2019a) and have been subsequently expanded to include additional surface pressure analysis.

2. Experimental setup

The experiments are conducted in a low-speed, low-turbulence open return wind tunnel located at the Flow Physics and Control Lab at Michigan State University. Flow enters the test section after passing through a series of screens, a

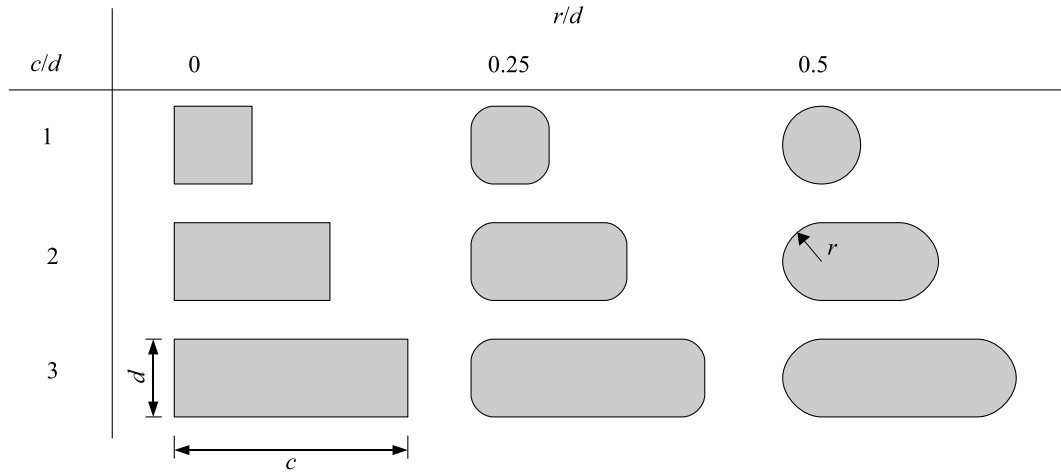


Fig. 2. Cross-sectional geometry of the models under investigation.

honeycomb and a 10:1 contraction. The test section has a 355 mm \times 355 mm square cross-section and is 3 m long. The mean turbulence intensity at the center of the test section over the range of freestream speeds used in this study is 0.1% for a frequency range above 0.5 Hz. The Reynolds number varies from $Re_d = 1100$ to 10,000, which corresponds to freestream velocities of approximately 0.8 m/s–7.5 m/s. The freestream velocity is monitored using a pitot-static tube connected to an MKS Baratron 223B differential pressure transducer with a full-scale range of 133 Pa and a 0.3% of-reading accuracy. At the low Reynolds number end, the pressure transducer resolution becomes a greater source of uncertainty than the accuracy, with a resolution of 0.013 Pa.

The experimental models under investigation are cylinders with nominally rectangular cross-section defined by the chord length c , the diameter $d = 20$ mm, and the corner radius r , as shown in Fig. 1. The coordinate s is the in-plane surface tangential direction, originating at the forward intersection of the chord line and the model surface. The cross-sectional shapes of the nine models are shown in Fig. 2. The case of $r/d = 0.5$ corresponds to cylinders with fully round fore and aft faces, while $r/d = 0$ is the sharp-cornered case. The models are 320 mm in length and span the majority of the test-section height, giving an aspect ratio of 16. The nominal solid blockage at an angle-of-attack $\alpha = 0^\circ$ is 5%, and the worst case blockage for $c/d = 3$ and $\alpha = 15^\circ$ is 10%. Circular end plates with a diameter of $15d$ and a 30° chamfered edge are fixed to the walls of the tunnel at each end of the model (Fig. 3(a)). In order to allow free movement of the model under aerodynamic loading for force measurements, a 30 mm long by 20 mm wide slot is necessary in the end plates. Initial testing showed that outside air drawn into the test-section through this slot had significant impact on the flow. As such, 4.5 d diameter, 0.75 mm thick fences are attached to the ends of the model to eliminate the unwanted axial flow. The diameter of the fences was selected by measuring drag and/or lift forces on several models with increasing fence diameter and determining the diameter at which the measured forces reached a plateau. The added drag due to the fences is estimated by assuming a skin friction drag equivalent to that of a turbulent flat plate with the same area. Based on this assumption, the worst case overestimation in the drag coefficient of the model is 0.04 at $Re_d = 1000$. A gap of approximately 0.5 mm is maintained between the fences and the fixed end plates, as shown in Fig. 3(a).

The models are constructed using one of two methods. For geometries where only force measurements are performed, the model is machined from a single piece of aluminum. When surface pressure measurements are desired, the model is made in three spanwise segments; two outer aluminum segments, and a center 3D printed segment housing the pressure taps. Pressure taps with a diameter of 0.35 mm are distributed around the perimeter of the model with a typical spacing in the s -direction of $0.02 P$, where P is the model perimeter. Where necessary, the spanwise locations of successive taps are staggered to accommodate the connection of plastic tubing inside the model. For the $c/d = 1$ models, only half the perimeter houses pressure taps due to limited space for tubing inside the model. In this case, full pressure distributions are measured by first measuring at α , and then $\alpha + 180^\circ$. A step-servo motor with a resolution of 0.02° is used to control α . The tubing is connected to a 48 channel Scanivalve multiplexer and the pressure is measured using an MKS Baratron 226A transducer with 133 Pa range. This sensor has a 0.3% of-reading accuracy and a resolution of 0.013 Pa. Data is sampled at 2 kHz with a typical sampling time of 120 s. This corresponds to a minimum sampling frequency and sampling time of $5U_\infty/d$ and $4800D/U_\infty$, respectively.

A custom one-component force balance is used to measure the lift and the drag forces on the model. For the Reynolds number range of interest, these forces are very low in magnitude. For example, at $Re_d = 1000$ a drag coefficient $C_D = 1$ corresponds to a force of approximately 2.5 mN given the model dimensions. The force balance, shown in Fig. 3(b), is comprised of a parallelogram four bar linkage from which the model is suspended. Given the length of the bars from which the moving plate is suspended, the balance moves primarily unidirectionally as the vertical displacement is $\mathcal{O}(10^2)$ – $\mathcal{O}(10^4)$

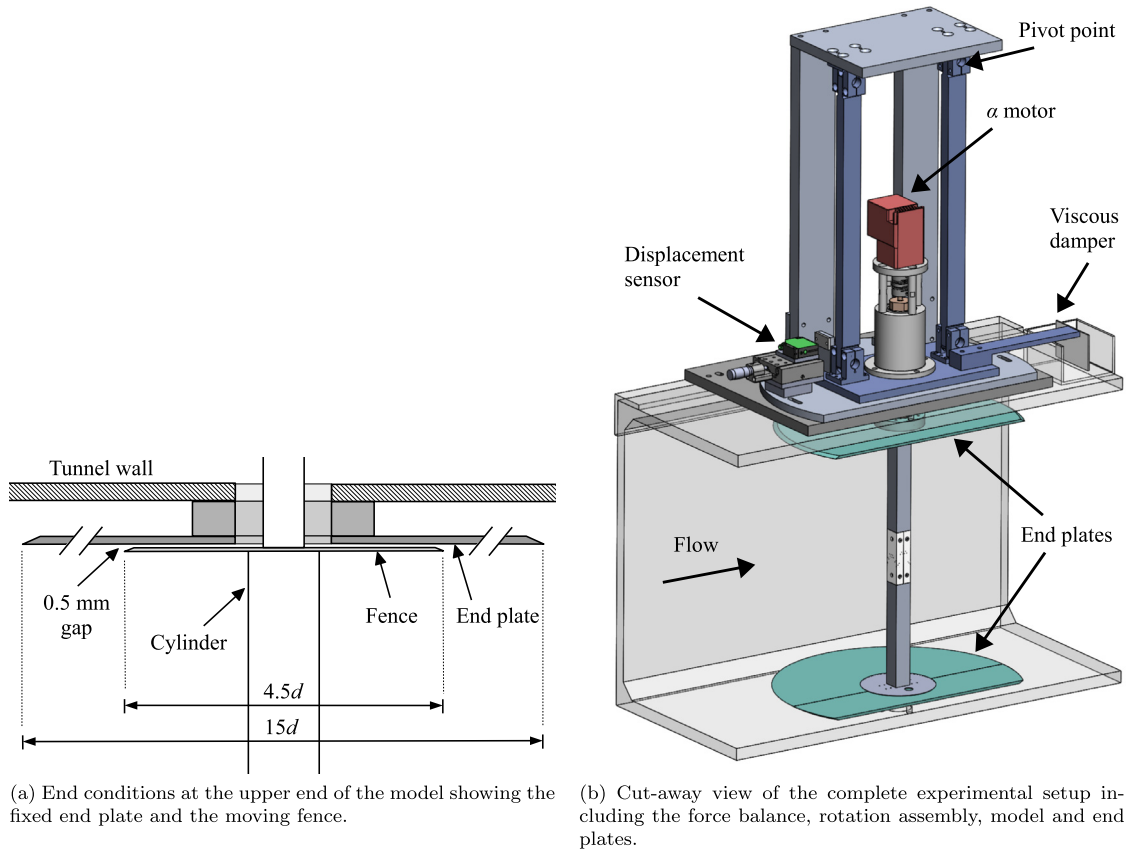


Fig. 3. Experimental setup schematics.

times smaller than the horizontal one. The angular motion at the pivot points is accomplished using Riverhawk 6016–600 rotational flexures that have no surface-on-surface contact, thus avoiding static-friction issues. The loads that oppose the motion of the balance and provide the necessary stiffness are the total suspended weight and the torque at the pivot points. By measuring the displacement of the balance in the force direction using a Baumer OADM 12U6430 non-contact triangulation laser displacement sensor (3–5 μm resolution), the force can be obtained if the stiffness is known. An *in-situ* calibration is performed by applying known loads and measuring the displacement. The balance is calibrated over a range of 2.5 mN–500 mN and a typical stiffness is 110 ± 1 N/m. Extensive calibrations have shown that the response of the balance is linear over the entire calibrated range. The full balance assembly is mounted to a platform that can be rotated to change between lift and drag measurement; the configuration in Fig. 3(b) shows the balance in the drag measurement position. A viscous damper, composed of a mesh plate in an oil reservoir, is necessary to damp the oscillations of the balance at its natural frequency of approximately 1 Hz. For a $c/d = 1$, $r/d = 0$ cylinder with a non-dimensional vortex shedding frequency of 0.13 (Noda and Nakayama, 2003), the expected shedding frequency is 4 Hz at $Re_d = 1000$. These oscillations have negligible effect on the mean forces as they are also very low in amplitude due to the damping of the balance, with a maximum amplitude of approximately 0.03 d at the highest Reynolds number. Given the stiffness of the force balance, which depends on model weight, and the resolution of the displacement sensor, a force resolution of approximately 0.2 mN is achieved. For C_D or C_L of 1, the typical accuracy of the force measurements ranges from 0.2 mN to 2.3 mN over $Re_d = 1100$ to 10,000. Complete details regarding the custom force balance, including a validation study, can be found in Feero et al. (2019b).

3. Results

3.1. Sharp-cornered square cylinder

Examples of the directly measured C_L and C_D variation with α are shown in Fig. 4 for the $c/d = 1$, $r/d = 0$ model. Five different Reynolds numbers are considered: $Re_d = 1100$, 2500, 5000, 7500 and 10,000. The ranges of measurement uncertainties in C_D and C_L are 0.02–0.07 and 0.002–0.06, respectively. For $Re_d > 1100$, the variation in C_D with α is

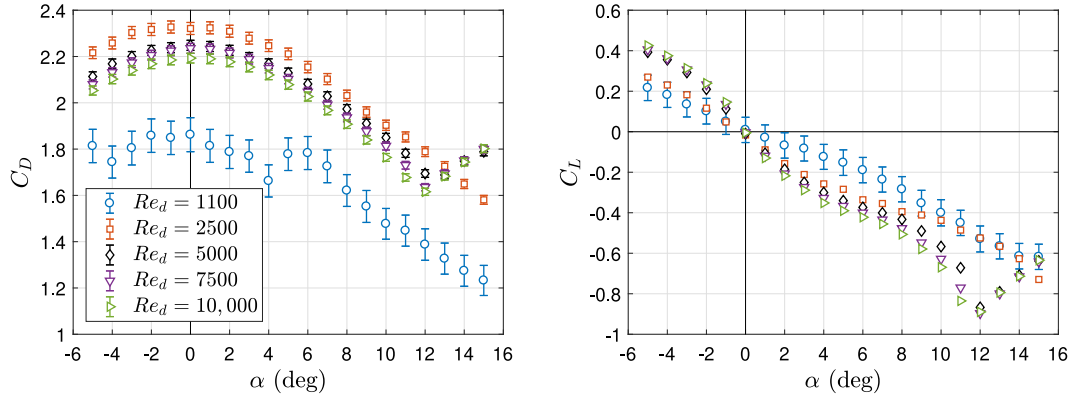


Fig. 4. Drag and lift coefficients for the $c/d = 1$, $r/d = 0$ cylinder as a function of angle-of-attack and Reynolds number. Other than $Re_d = 1100$, the error bars on C_L are less than the marker size.

approximately parabolic at low α , with a local maximum occurring at $\alpha = 0^\circ$. This behavior of a maxima in drag at $\alpha = 0^\circ$ was not consistent over the entire geometry range; although not shown for brevity, some of the models with larger c/d displayed the inverse trend of a local minimum in drag at $\alpha = 0^\circ$. When the Reynolds number is reduced to $Re_d = 1100$, there is a substantial decrease in C_D and a flattening of the curve for $-5^\circ \leq \alpha \leq 5^\circ$. Beyond this flat section, C_D continues to decrease with α up to 15° , which is similar to the behavior at $Re_d \geq 2500$. For $Re_d \geq 5000$, there is a drastic change in C_D at $\alpha = 12^\circ$ where the slope of the curve sharply reverses and drag begins to increase. This change with Reynolds number is also reflected in the lift coefficient, where C_L monotonically decreases with α for $Re_d < 5000$, but a reversal in the C_L slope occurs at $\alpha = 12^\circ$ for $Re_d \geq 5000$. The drastic change in C_D and C_L at $\alpha = 12^\circ$ is due to flow reattachment on the bottom face, which is a well known effect for square cylinders with $r/d = 0$ (e.g. Huang et al., 2010), and the angle where reattachment occurs is often referred to as the critical angle. This value of the critical angle and its insensitivity to Reynolds number agree very well with other studies who all found reattachment to occur at $\alpha = 12^\circ$ for $5000 \leq Re_d \leq 37,000$ (Carassale et al., 2014; Luo et al., 1994; Norberg, 1993). The presence of a negative C_L slope at each Reynolds number indicates the possibility of galloping, since it can be shown that $\partial C_y / \partial \alpha > 0$ is equivalent to $\partial C_L / \partial \alpha + C_D < 0$ for small α (Blevins, 2001).

Prior to considering the results for the other geometries, the galloping behavior of the $c/d = 1$, $r/d = 0$ case will first be discussed since there exists data regarding this geometry from previous studies. Fig. 5(a) shows the variation in the normal force with α computed using C_D and C_L from Fig. 4. As discussed in Section 1, the sign of $\partial C_y / \partial \alpha$ indicates stability with respect to transverse galloping. In particular, a shape is deemed “unstable” with respect to galloping when $\partial C_y / \partial \alpha > 0$ at $\alpha = 0^\circ$, since this corresponds to a body galloping from rest. If $\partial C_y / \partial \alpha < 0$ at $\alpha = 0^\circ$, but the slope in C_y is positive at some α range away from 0° , the body can still gallop as a hard oscillator. Hard galloping will be discussed in a subsequent section. The results in Fig. 5(a) demonstrate that for $Re_d > 1100$, $\partial C_y / \partial \alpha > 0$ at $\alpha = 0^\circ$ and the body is unstable. At $Re_d = 1100$, the change in C_y near $\alpha = 0^\circ$ is negligible within the error bounds, thus the body is neutrally stable at this Reynolds number. Fig. 5(a) also includes a comparison with the C_y data from Norberg (1993) and Bearman et al. (1987) at $Re_d = 13,000$ and $14,000$, respectively. Very good agreement is observed between these studies and the present data at $Re_d = 10,000$. The severity of the galloping instability can be quantified by examining the magnitude of $\partial C_y / \partial y$, which is shown in Fig. 5(b) for $\alpha = 0^\circ$. The derivative was computed from either a cubic spline fit of C_y , or a sliding cubic fit for $Re_d < 5000$ to smooth the scatter in the data. Over $1100 \leq Re_d \leq 10,000$, the derivative of C_y increases monotonically from a value that is zero (within uncertainty) to 6.4 ± 1.9 . This indicates that the cylinder becomes more susceptible to galloping with increasing Reynolds number. Data from previous studies up to $Re_d = 66,000$ are also included in this figure for comparison with the present results. The only value of $\partial C_y / \partial \alpha$ that overlaps the present Reynolds number range is from Norberg (1993) at $Re_d = 5000$, which agrees within uncertainty with the present value of $\partial C_y / \partial \alpha$ at the same Re_d . The combination of the data from this study and that of other researchers shows a maximum in $\partial C_y / \partial y \approx 6$ at $Re_d \approx 10,000$, with the value at higher Reynolds number potentially plateauing at $Re_d \approx 30,000$ at a value of $\partial C_y / \partial y = 2 - 3$. It is often assumed that the effect of Reynolds number on the galloping behavior of rectangular cylinders with $r/d = 0$ is negligible due to their fixed separation points (e.g. Piccardi et al., 2011). However, the present results and those of other studies demonstrate that quite the opposite is true for $c/d = 1$ when the Reynolds number is sufficiently low.

3.2. Normal force coefficients and galloping behavior

The C_y variation with α and Re_d for each of the geometries shown in Fig. 2 is shown in Figs. 6–8 for $c/d = 1, 2$ and 3 , respectively. The $c/d = 1, r/d = 0.5$ case is not shown since this geometry is stable by definition. The results are grouped by c/d since the maximum value of C_y increases substantially with increasing c/d for each r/d .

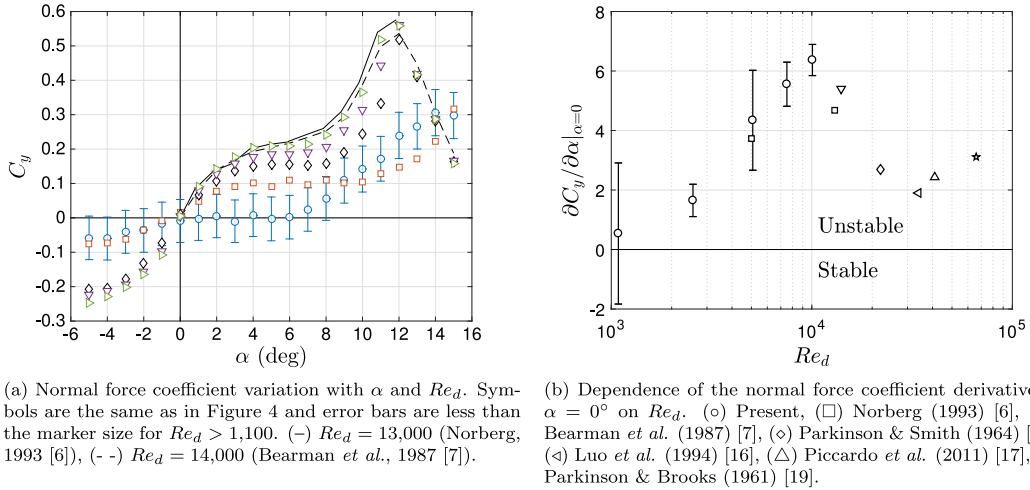


Fig. 5. Galloping stability for $c/d = 1$, $r/d = 0$ (Parkinson and Brooks, 1961; Parkinson and Smith, 1964).

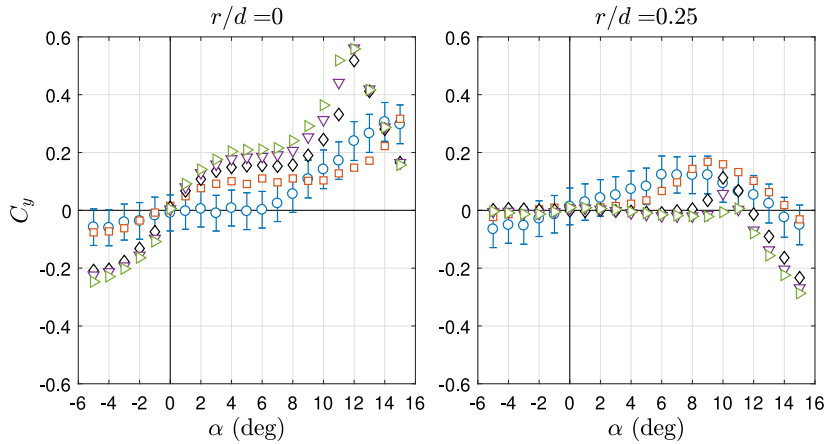


Fig. 6. Normal force coefficient variation with α and Re_d for $c/d = 1$. (○) $Re_d = 1100$, (□) $Re_d = 2500$, (◇) $Re_d = 5000$, (▽) $Re_d = 7500$, (△) $Re_d = 10,000$.

The results for $c/d = 1$, shown in Fig. 6, will first be considered. The previously shown plot of C_y for $c/d = 1$, $r/d = 0$ is reproduced in this figure for direct comparison with $r/d = 0.25$. After the region of positive $\partial C_y / \partial \alpha$ for $r/d = 0$ and $Re_d > 2500$, the slope becomes flat for $\alpha \approx 4^\circ$ to 7° , prior to increasing once again up to the critical angle of 12° . Beyond this angle, the slope in C_y becomes negative and the body is stable. $Re_d = 2500$ displays a similar trend, however there is no reattachment at this Reynolds number and $\partial C_y / \partial \alpha$ remains positive after $\alpha = 10^\circ$. Comparing C_y for $r/d = 0.25$ to $r/d = 0$, a drastic change is observed. At this increased value of r/d , the slope in C_y near $\alpha = 0^\circ$ is zero for $Re_d > 1100$, indicating the body is neutrally stable. A slight positive slope is observed for $Re_d = 1100$, although given the error bounds on C_y , the slope may still be very near zero. For $2500 \leq Re_d \leq 7500$, an α range away from zero is observed where $\partial C_y / \partial \alpha$ becomes positive, and this range both shrinks in size and becomes farther from $\alpha = 0^\circ$ with increasing Reynolds number. After this range of positive $\partial C_y / \partial \alpha$, C_y begins to decrease and the body is stable. Once $Re_d = 10,000$ is reached, C_y is essentially flat up to $\alpha = 11^\circ$, after which $\partial C_y / \partial \alpha < 0$. These results demonstrate that for $c/d = 1$, the corner radius has a profound effect on galloping behavior and the resistance of a cylinder with unity side ratio to galloping can be improved by increasing r/d .

The variation in C_y with α for $c/d = 2$ is shown in Fig. 7 for $r/d = 0, 0.25$ and 0.5 . For $r/d = 0$, the results are reminiscent of those for $c/d = 1$ at the same r/d , although at this larger side ratio $\partial C_y / \partial \alpha$ is positive at $\alpha = 0^\circ$ for the entire Reynolds number range. The C_y curves also show a sharp change from $\partial C_y / \partial \alpha > 0$ to $\partial C_y / \partial \alpha < 0$ at a lower angle-of-attack than for $c/d = 1$. This angle decreases from approximately 8° to 6° with increasing Re_d , and it is possible that this represents similar flow reattachment behavior as for $c/d = 1$. Unlike the variation in C_y for $c/d = 1$, there is no region of flat C_y and $\partial C_y / \partial \alpha$ is positive for all α prior to the sharp change in slope. As r/d is increased to 0.25 for $c/d = 2$, substantially different trends are observed. A much stronger dependence on Reynolds number is observed for

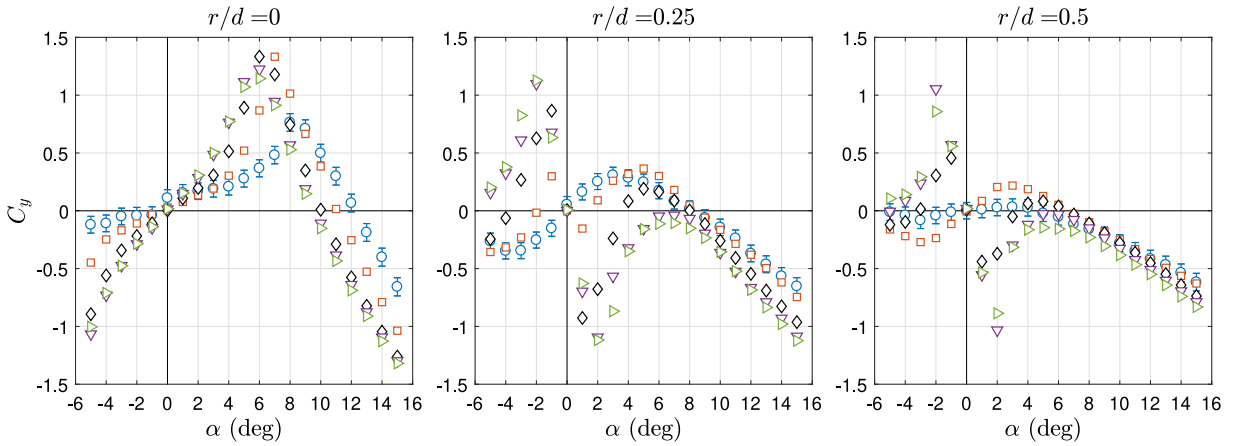


Fig. 7. Normal force coefficient variation with α and Re_d for $c/d = 2$. Symbols are the same as in Fig. 6.

this geometry, as the slope in C_y at $\alpha = 0^\circ$ is positive for $Re_d = 1100$, but becomes negative at $Re_d = 2500$ and increasingly so with increasing Re_d . Interestingly, increasing r/d to 0.25 has a weaker effect on the slope of C_y at $\alpha = 0^\circ$ at $Re_d = 1100$ compared with other Reynolds numbers. The local minimum value of C_y for $Re_d > 1100$ increases in magnitude with Re_d , along with a slight increase in the α value corresponding to the peak. After this local minimum in C_y , each of these cases shows a range of α over which a strong positive gradient in C_y is observed, followed by a smooth transition to a negative gradient at high angle-of-attack. Similar to $r/d = 0$, at high angle-of-attack, the effect of Reynolds number decreases and C_y begins to decrease at a comparable rate for all Re_d . The behavior of C_y at $r/d = 0.5$ is qualitatively similar to that of $r/d = 0.25$. The most notable difference at this maximum value of r/d is that the slope in C_y at $\alpha = 0^\circ$ varies from flat at $Re_d = 1100$, to slightly positive at $Re_d = 2500$, to negative for all higher Re_d . For $Re_d \geq 7500$, the minimum value of C_y is very close to that at $r/d = 0.25$, and it also occurs at $\alpha = 2^\circ$. Once again, a consistent trend that is observed is that Reynolds number effects weaken at high α , where in this case C_y data almost collapse for all Re_d .

The remaining plots of C_y for the largest side ratio under investigation, $c/d = 3$, are shown in Fig. 8. The results for $c/d = 3$, $r/d = 0$ bear resemblance to those of $c/d = 2$, $r/d > 0$, where $\partial C_y / \partial \alpha$ at $\alpha = 0^\circ$ shows a strong dependance on Reynolds number. For this geometry, the slope of C_y near zero angle-of-attack is positive and the body is unstable for $Re_d \leq 2500$, but becomes negative and stable for larger Reynolds number. A smooth transition from positive to negative C_y slope with increasing α is observed for $Re_d = 1100$, whereas a sharp transition occurs for $Re_d = 2500$. For $Re_d > 2500$, C_y is negative for all positive α , and only a small α range can be seen where C_y increases at a relatively low rate. The effect of Reynolds number on C_y undergoes a change once the corner radius is increased above $r/d = 0$, where for both $r/d = 0.25$ and 0.5 the slope of C_y near $\alpha = 0^\circ$ becomes exclusively negative for all Re_d . In addition to this, the peak values of C_y show a significant increase compared to $r/d = 0$, with values of C_y reaching as large as nearly 3 in some cases. In fact, the general shape of C_y (which is approximately equal to $-C_L$ for small α) for $c/d = 3$ and $r/d \geq 0.25$ is much more reminiscent of that of a streamlined body than that of the other bluff bodies in this study. That is; C_y decreases approximately linearly near $\alpha = 0^\circ$ and $C_y < 0$ for $\alpha > 0$, with only a moderate increase in C_y following the peak minimum before decreasing once again. An interesting double peak behavior is observed for $r/d = 0.5$ and $Re_d \geq 7500$ that is not seen for any other cases. This side ratio also demonstrates consistent behavior where the slope in C_y becomes relatively insensitive to Reynolds number at high angle-of-attack.

The effects of c/d and r/d on the galloping criterion, $\partial C_y / \partial \alpha|_{\alpha=0}$, over the Reynolds number range investigated are highlighted in Figs. 9 and 10, respectively. Considering first the effects of c/d on galloping, Fig. 9 shows that for $r/d = 0$, $\partial C_y / \partial \alpha|_{\alpha=0}$ shows a very similar trend of increasing with Reynolds number for both $c/d = 1$ and 2. In fact, over much of the Re_d range, the values of $\partial C_y / \partial \alpha|_{\alpha=0}$ are within uncertainty of each other for these two side ratios. Once c/d increases to 3, the galloping behavior changes substantially as there is a transition from instability to stability between $Re_d = 2500$ and 5,000. For $Re_d < 5000$ where $\partial C_y / \partial \alpha|_{\alpha=0} > 0$, the derivative is an order of magnitude larger for $c/d = 3$, and this body is thus substantially more unstable than $c/d = 1$ and 2. At $r/d = 0.25$, there is no longer similar behavior between $c/d = 1$ and 2, as $c/d = 1$ is neutrally stable for all Re_d , whereas $c/d = 2$ transitions from unstable to stable between $Re_d = 1100$ and 2500. A similar transitional behavior for $c/d = 2$ occurs for $r/d = 0.5$, although in this case at a larger Reynolds number. Once c/d is increased to 3 for both $r/d = 0.25$ and 0.5 , these geometries become stable over the entire Reynolds number range. A similarity that can be observed for both $r/d = 0.25$ and 0.5 is that the $\partial C_y / \partial \alpha|_{\alpha=0}$ curves for $c/d = 2$ and 3 appear to converge as Re_d approaches 10,000.

The effects of r/d on the galloping criterion are shown in Fig. 10. An overarching observation that can be made for all side ratios is that increasing the corner radius has a stabilizing effect. That is, increasing r/d from 0 to 0.5 can cause the cylinder to transition from unstable to stable at a given Reynolds number. For example, $c/d = 1$ shows this trend at

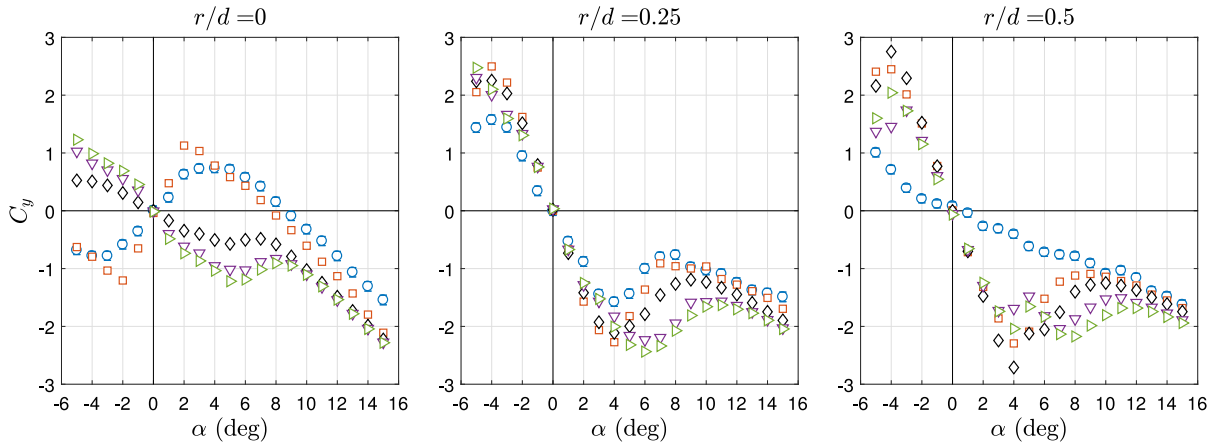


Fig. 8. Normal force coefficient variation with α and Re_d for $c/d = 3$. Symbols are the same as in Fig. 6.

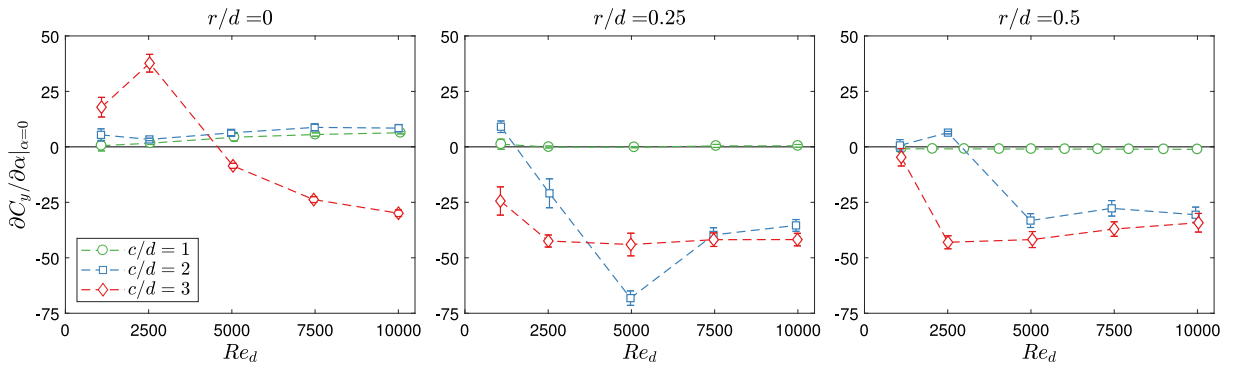


Fig. 9. Side ratio effect on the galloping criterion at $\alpha = 0^\circ$ as a function of Reynolds number.

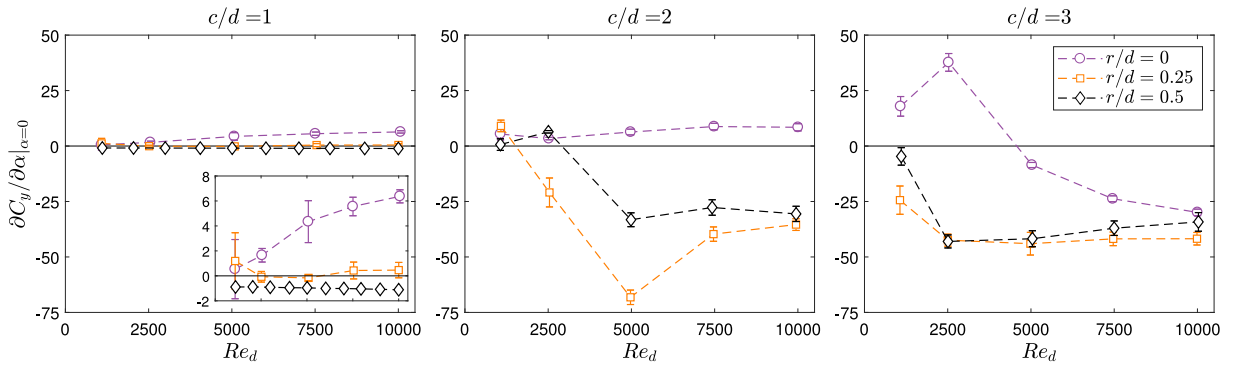


Fig. 10. Corner radius effect on the galloping criterion at $\alpha = 0^\circ$ as a function of Reynolds number. The inset plot for $c/d = 1$ has a reduced ordinate scale to highlight the r/d effects.

$Re_d = 10,000$. However, for $c/d = 1$ and 2 this stabilizing behavior has a diminishing effect with decreasing Reynolds number, where the value of $\partial C_y / \partial \alpha|_{\alpha=0}$ tends towards 0 for most r/d values. The opposite behavior occurs at $c/d = 3$ where the stabilizing effect of r/d is most pronounced for $Re_d < 5000$, while the effect of r/d becomes negligible at the high Reynolds number end.

A number of previous studies have investigated the transverse galloping behavior of rectangular cylinders with sharp corners, $r/d = 0$. The present values of $\partial C_y / \partial \alpha|_{\alpha=0}$ as a function of c/d are compared with data from literature for $Re_d \geq 1 \times 10^4$ in Fig. 11. In this Reynolds number range, the flow is expected to become relatively insensitive to Re_d due to fixed separation points at the sharp corners. Fig. 11 demonstrates that the present results agree well with those

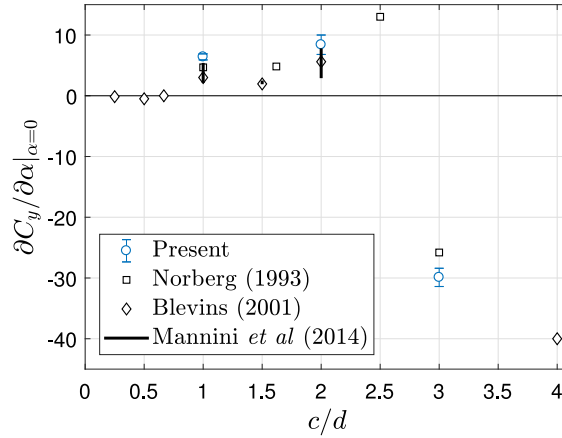


Fig. 11. Comparison of the galloping criterion dependence on c/d for sharp-cornered ($r/d = 0$) rectangular cylinders at $Re_d \geq 1 \times 10^4$ in smooth flow. The data from Blevins (2001) is based on tabulated data from several previous studies. The vertical lines indicate the range of $\partial C_y / \partial \alpha|_{\alpha=0}$ at a particular c/d from a number of previous studies, as summarized in the review by Mannini et al. (2014). All cases are based on experimental measurements.

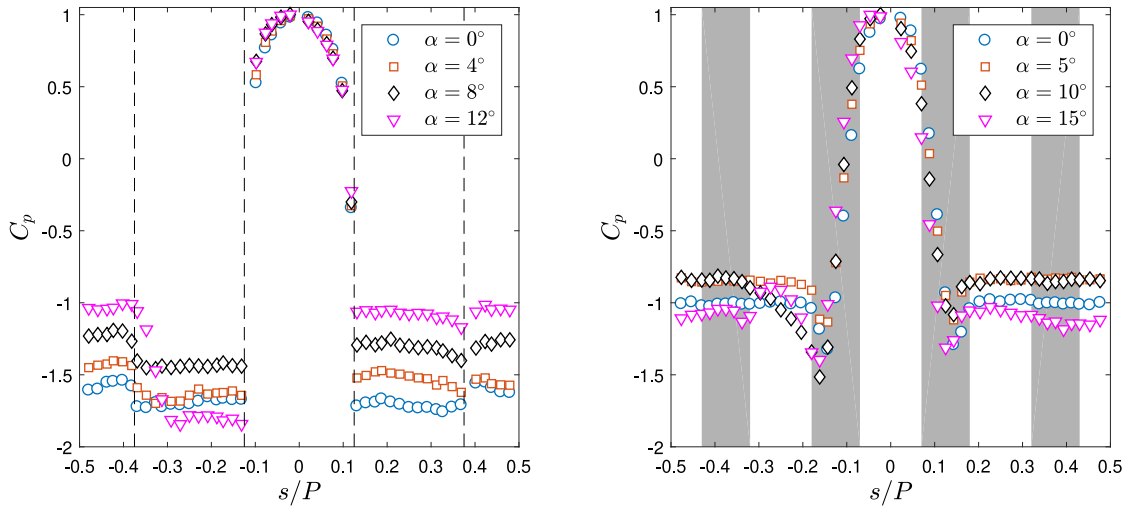
of previous studies; in particular, there is good agreement between the present results and those of Norberg (1993) for $c/d = 1$ and 3. Fig. 11 also highlights that a range of instability exists over $0.67 < c/d < 3$, with the most unstable geometry likely occurring between $c/d = 2$ and 3. The data included from the review by Mannini et al. (2014) highlight the fact that for $c/d = 1$ and 2, there is a considerable range of $\partial C_y / \partial \alpha|_{\alpha=0}$ reported in various studies. This is likely the result of experimental differences, such as boundary conditions and actual r/d (i.e., how close r/d is to zero), as well as the uncertainty in computing the derivative from experimental data. In addition to this, $\partial C_y / \partial \alpha|_{\alpha=0}$ may plateau at a Reynolds number larger than $Re_d \approx 10,000$, as evidenced by the data in Fig. 5(b) for $c/d = 1$.

3.3. Surface pressure distributions

Further insight into the effects of cylinder geometry on the flow can be gained by considering surface pressure distributions for select cases. Figs. 12 and 13 show the variation in $C_p = (p - p_\infty)/q_\infty$ over the surface, where p and p_∞ are the surface and freestream static pressure, respectively. The pressure coefficient is plotted against the wall-tangential coordinate s normalized by the perimeter, P . The cases selected for examining C_p are $c/d = 1$, $r/d = 0$ and 0.25 (Fig. 12), and $c/d = 3$, $r/d = 0$ (Fig. 13). The geometry, Re_d and α cases were selected to investigate the cause of different $\partial C_y / \partial \alpha$ behaviors (i.e., α regions of negative, approximately zero, or positive $\partial C_y / \partial \alpha$).

Surface pressure distributions at several angles-of-attack and $Re_d = 5000$ for $c/d = 1$, $r/d = 0$ are shown in Fig. 12(a). In this plot, the dashed vertical lines identify the locations of the corners. As per the definition in Fig. 1, $s = 0$ originates at the center of the front face and increasing s travels along the cylinder surface in the clockwise direction. At $\alpha = 0^\circ$, the C_p distribution shows that other than the front face, the flow is separated over the remaining three faces, as indicated by an approximately constant C_p on each of these faces. Once α increases to 4° , the flow remains separated on these faces, however the pressure increases on the upper face ($0.13 \leq s/P \leq 0.38$) but is relatively unchanged on the lower face ($-0.38 \leq s/P \leq -0.13$). This change in the pressure level of the separated flow between the upper and lower faces as α increases from 0° to 4° leads to an increase in C_y and thus instability with respect to galloping, as shown in Fig. 5(a). As α increases further to 8° , the flow remains separated and the pressure level increases by a similar amount on both the upper and lower faces, leading to approximately no change in C_y . The local maximum in C_y at $\alpha = 12^\circ$ coincides with the flow on the bottom face reattaching near the corner at $s/P = -0.38$, as was expected from previous discussion. Flow reattachment on the bottom face is indicated by the region of substantial pressure recovery that follows the region of separated flow after the $s/P = -0.13$ corner. The flow then separates again from the rear corner over the back face.

Similar results are presented for comparison in Fig. 12(b) for the $c/d = 1$, $r/d = 0.25$ cylinder. For this geometry, the curved faces at the corners are indicated by shaded regions on the plot. The flow at $\alpha = 0^\circ$ is attached over the front corners ($0.07 \leq |s/P| \leq 0.18$) and separates immediately following this. The point of separation is indicated approximately by the location where the gradient in C_p goes to zero (Yarusevych et al., 2006). Compared with $r/d = 0$, the value that C_p plateaus to near the rear of the cylinder is substantially larger, which is consistent with lower drag for $r/d = 0.25$. As α increases to 5° , there is a uniform increase in the C_p level over the regions past the top/bottom corners: $-0.5 \leq s/P \leq -0.18$ and $0.18 \leq s/P \leq 0.5$. Unlike $r/d = 0$ where the small α increase leads to relatively little change in C_p on the front face, there are substantial changes in C_p over the front face and front corners for $r/d = 0.25$. Specifically, the pressure decreases over the upper corner and similarly increases over the lower corner; however, the sum of all these changes is no change in C_y relative to $\alpha = 0^\circ$ (Fig. 6). A substantial change occurs at $\alpha = 10^\circ$ where



(a) $r/d = 0$. Dashed vertical lines indicate the corners.

(b) $r/d = 0.25$. Shaded areas indicate the curved corner faces.

Fig. 12. Surface pressure distributions at various angles-of-attack for $c/d = 1$ and $Re_d = 5000$.

the pressure minimum decreases at $s/P = -0.18$ and the flow appears to remain attached over a greater extent of the cylinder's lower half, separating near the beginning of the lower back corner ($s/P = -0.32$). This coincides with the local maximum in C_y . At $\alpha = 15^\circ$ the behavior remains similar with separated flow after the first corner on the upper half of the model, and attached flow on the bottom half up to the rear corner, which coincides with C_y decreasing and the body becoming stable.

The effect of increasing c/d to 3 for $r/d = 0$ is shown in Fig. 13 for $Re_d = 1100$, 5000 and 10,000. Unlike the $c/d = 1$, $r/d = 0$ geometry where $\partial C_y / \partial \alpha|_{\alpha=0} \geq 0$, $\partial C_y / \partial \alpha|_{\alpha=0}$ changes from negative to positive over the investigated Reynolds number range (Fig. 8). A general feature that can be observed for all Reynolds numbers for $c/d = 3$ is that after separation occurs at the front corners ($|s/P| = 0.06$), the flow reattaches at some point near the back corner ($|s/P| = 0.44$) on the top and bottom faces for $\alpha = 0^\circ$. This is indicated by the region of flat C_p followed by a monotonic pressure increase as the back corner is approached. The extent of the separated region on the top and bottom faces decreases with increasing Reynolds number.

Increasing from $\alpha = 0^\circ$ to 5° at $Re_d = 1100$ leads to very little change in the flow over the bottom surface of the cylinder, while the flow over the upper surface becomes fully separated. In addition, there is a substantial increase in the separation zone pressure relative to $\alpha = 0^\circ$. Similar to the results for $c/d = 1$, $r/d = 0$ at $Re_d = 5000$, no change in the flow on the bottom face and an increase in separation zone pressure on the upper face leads to an increase in C_y , thus making the body unstable. As α increases to 8° , the separated flow on the upper surface is unchanged, while on the bottom face it appears that the flow is either fully attached or the separation zone has shrunk considerably. This is indicated by a region of positive pressure gradient from the front corner up to $s/P = -0.36$. However, given the error bounds on C_p at this Re_d , it is not possible to determine whether the pressure is truly increasing over approximately $-0.2 \geq s/P \geq -0.1$. Irrespective of this fact, the reduced region of separated flow leads to a decrease in C_y relative to $\alpha = 5^\circ$. The C_p distribution shows a marked change at the largest α of 15° , where there is a relatively strong positive gradient in C_p originating at the front corner, which indicates attached flow. This is followed by a region of flat C_p over approximately $-0.25 \geq s/P \geq -0.15$, and finally a decrease in C_p towards the back corner. This region of flat C_p suggests the possibility of a small separation bubble on the lower surface. The large increase in C_p over the majority of the bottom face leads to a further decrease in C_y relative to $\alpha = 8^\circ$.

The C_p results for $Re_d = 5000$ are shown in Fig. 13(b). As α is increased from 0° to 5° , the flow becomes fully separated on the upper face but on the bottom face the region of separated flow shrinks in length, as indicated by a shorter extent of C_p that is approximately constant. In addition to this, the rate of pressure recovery increases and a local maximum appears in the C_p distribution on the bottom face. The flow over one of the cylinder's front corners resembles that of a canonical backwards facing step, for which it has been shown that reattachment occurs near the point of maximum C_p (Le et al., 1997). Therefore, the location of the C_p maximum can be used as an indication of the reattachment location. Unlike $c/d = 1$ where a small increase in α from 0° causes the flow to remain separated on the top and bottom faces and an increase in C_y , a shrinking of the separated region for $c/d = 3$ is responsible for the decrease in C_y (Fig. 8) and stability with respect to galloping. At $\alpha = 8^\circ$, C_y increases slightly relative to $\alpha = 5^\circ$ and similarly there appears to be very little change in the length of the separated region on the bottom face, although the pressure recovery rate does increase. The separated region shrinks in size as α increases to 15° and there is a substantial increase in the separation zone pressure, leading to a

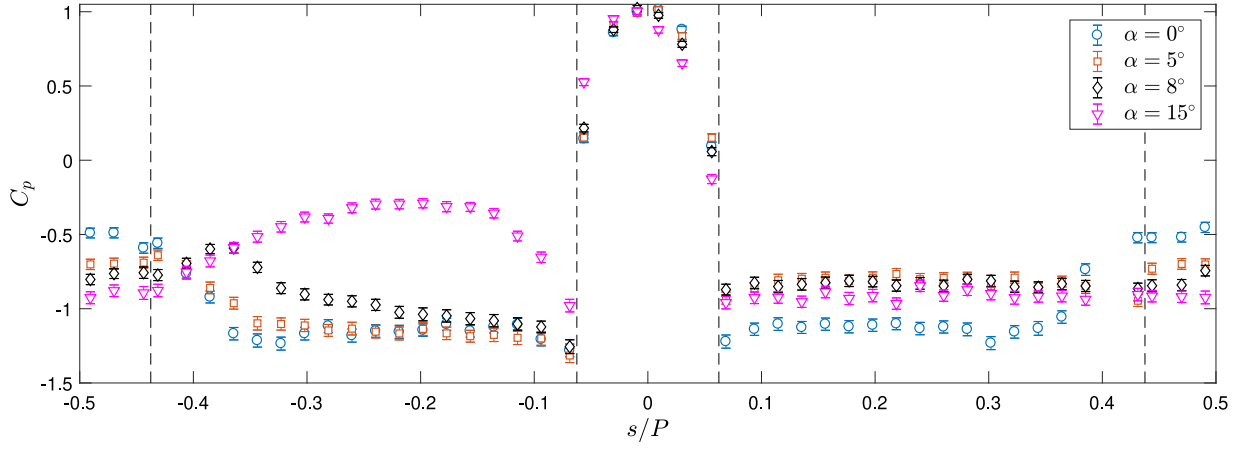
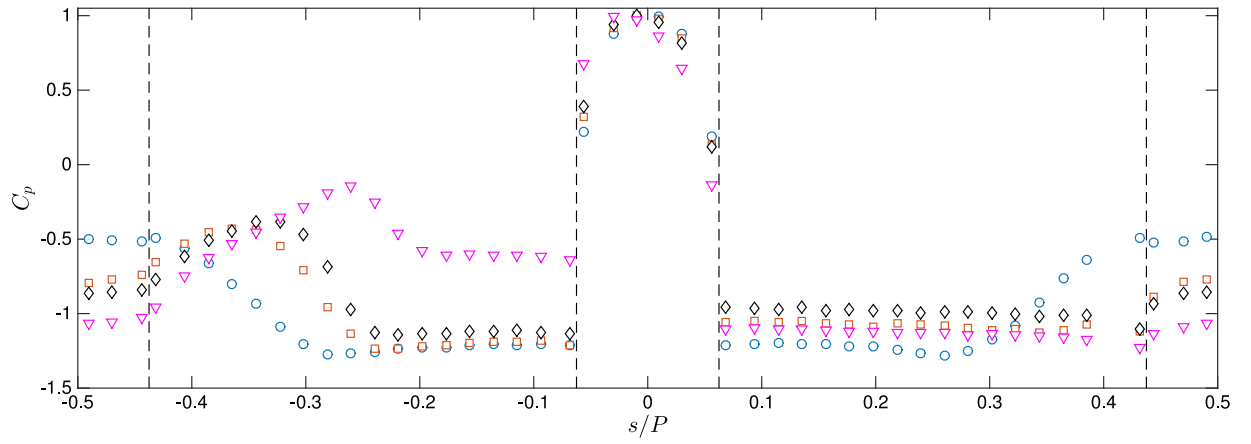
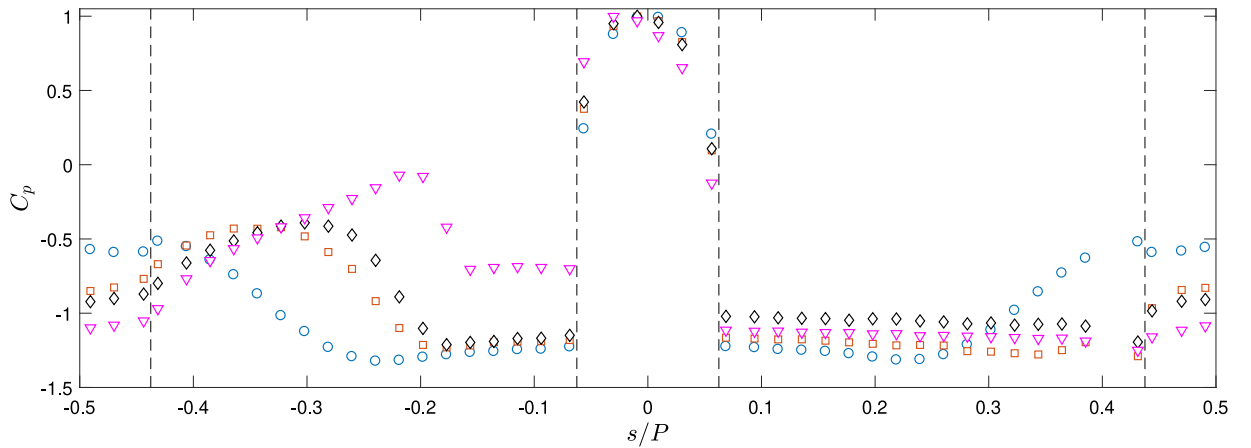
(a) $Re_d = 1,100$ (b) $Re_d = 5,000$ (c) $Re_d = 10,000$

Fig. 13. Surface pressure distributions at various angles-of-attack for $c/d = 3$, $r/d = 0$. Dashed vertical lines indicate the corners. Error bars are less than the marker size for $Re_d > 1100$.

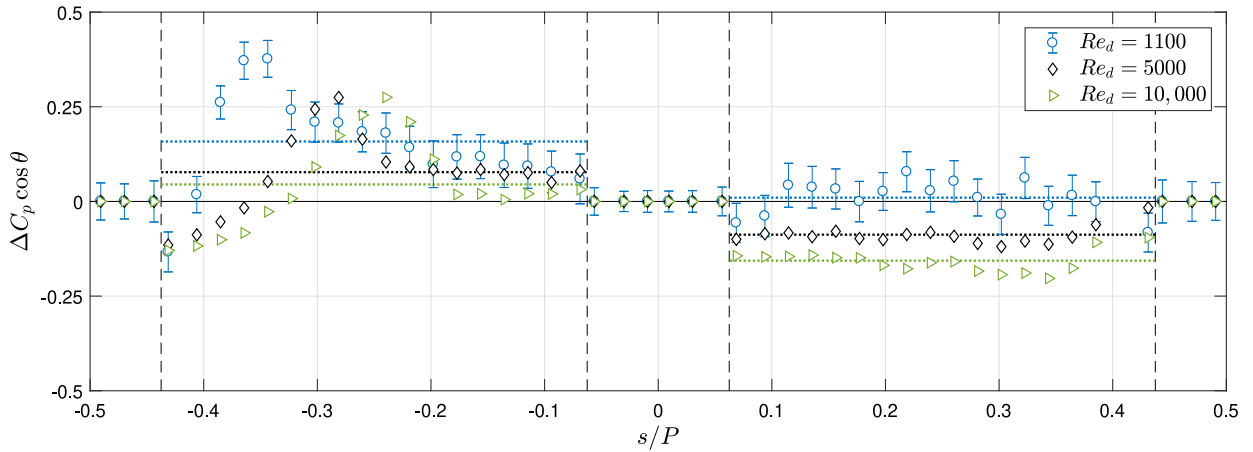


Fig. 14. Surface pressure difference between $\alpha = 8^\circ$ and 5° for $c/d = 3$, $r/d = 0$. C_p is multiplied by $\cos \theta$, which represents the contribution of C_p to the normal force. The dashed horizontal lines are the average values of $\Delta C_p \cos \theta$ over the indicated s range.

large decrease in C_y . It is interesting to note for $\alpha = 15^\circ$ at $Re_d = 5000$ and $10,000$, the flow separates at each of the front corners, however at $Re_d = 1100$ the flow remains attached over the bottom front corner ($s/P = -0.06$). It is hypothesized that this is a viscous effect related to the thickness of the boundary layer on the front face. From the Falkner–Skan solution for plane stagnation flow (White, 1974), the stagnation point boundary layer thickness at $Re_d = 10,000$ can be estimated as $\sim 0.02d$, whereas at $Re_d = 1100$ it increases to $\sim 0.06d$. The thicker boundary layer approaching the corner may lead to an effective rounding of the corner (i.e., increased r/d), thereby mitigating flow separation.

The C_y results for $r/d = 0$ in Fig. 8 show that over $5^\circ \leq \alpha \leq 8^\circ$, there are distinct differences between $Re_d = 1100$, 5000 and $10,000$. In particular, in this range C_y decreases with α by ~ 0.6 at $Re_d = 1100$, is approximately flat at $Re_d = 5000$, and increases by ~ 0.3 at $Re_d = 10,000$. These three different qualitative trends, caused by changing the Reynolds number, correspond to stability, neutral stability, and instability to galloping, respectively. The cause of these different behaviors can be investigated by considering the contribution of surface pressure to C_y , viz.

$$C_{y,p} = - \int_p C_p \cos \theta \, d\left(\frac{s}{d}\right), \quad (2)$$

where θ is the local angle between the surface and the cylinder chordline. The difference in $C_p \cos \theta$ between $\alpha = 8^\circ$ and 5° , $\Delta C_p \cos \theta$, is shown in Fig. 14 for each Reynolds number. Also included in this plot are dashed horizontal lines that indicate the average value of $\Delta C_p \cos \theta$ over a given face, thus representing the contribution to $\Delta C_{y,p}$. At $Re_d = 1100$, there is no change in C_p on the top face and the observed decrease in C_y is due entirely to C_p increasing over the bottom face due to earlier reattachment at $\alpha = 8^\circ$, as discussed in Fig. 13(a). The surface pressure on the bottom face also generally increases at $Re_d = 5000$ due to slightly earlier reattachment at $\alpha = 8^\circ$, but the pressure also increases over the entire top face. The average value of $\Delta C_p \cos \theta$ is of approximately equal magnitude but opposite sign (since θ differs by 180°) for these two faces, therefore there is no change in C_y . Comparing with $Re_d = 5000$, at $Re_d = 10,000$ the average value of $\Delta C_p \cos \theta$ on the bottom surface becomes less positive, while on the top surface it becomes increasingly negative due to a larger increase in the separation zone pressure. Thus, the primary cause of the difference in the C_y behavior from $\alpha = 5^\circ$ to 8° between $Re_d = 5000$ and $10,000$ is the change in separation zone pressure on the top face, with a smaller contribution from the flow over the bottom face.

The surface pressure distribution results discussed in this section show that galloping stability versus instability (i.e., the sign of $\partial C_y / \partial \alpha$) is related to whether the region of separated flow on the bottom face of the cylinder decreases or not with increasing angle-of-attack, where the former case results in stability. A shrinking of the separation zone leading to $\partial C_y / \partial \alpha < 0$ is observed at both low and high α depending on the geometry and Reynolds number. In cases where the flow on the bottom face is relatively unchanged with increasing α (e.g., $c/d = 1$, $r/d = 0$ between $\alpha = 0^\circ$ and 4° at $Re_d = 5000$, as shown in Fig. 12(a)), instability is associated with an increase in the separation zone pressure on the upper face.

3.4. Hard galloping

As shown in Section 3.2, there are certain geometries that are stable with respect to galloping at $\alpha = 0^\circ$ (i.e., $\partial C_y / \partial \alpha|_{\alpha=0} < 0$) but still exhibit ranges of α where $\partial C_y / \partial \alpha > 0$, thereby making them susceptible to hard galloping. For a more detailed description of the hard galloping phenomenon, the reader is directed to Blevins (2001) and Naudascher and Rockwell (2005). Ranges of α where $\partial C_y / \partial \alpha > 0$ are observed for $c/d = 2$ and 3 , with dependence on Re_d and r/d . The

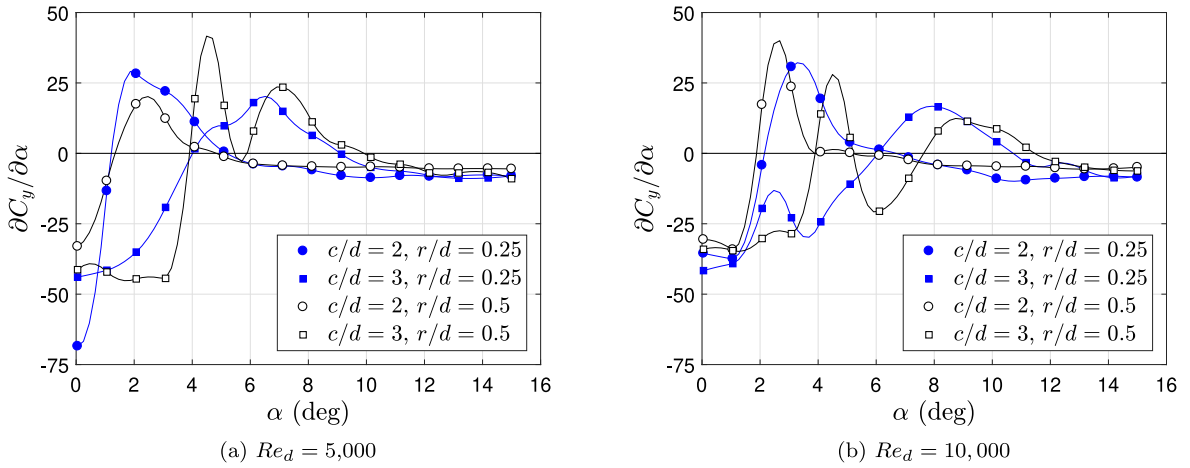


Fig. 15. Galloping criterion versus angles-of-attack for $c/d = 2$ and 3 , $r/d = 0.25$ and 0.5 at $Re_d = 5000$ and $10,000$. Filled markers indicate $r/d = 0.25$, open markers indicate $r/d = 0.5$.

behavior of $\partial C_y/\partial\alpha$ over $0 \leq \alpha \leq 15^\circ$ is shown in Fig. 15 for four cases with two side ratios and two corner radii: $c/d = 2$ and 3 , and $r/d = 0.25$ and 0.5 . The results demonstrate for each of these four geometries, there are one to two ranges of α where $\partial C_y/\partial\alpha > 0$ and the body could exhibit hard galloping. At $Re_d = 5000$, the $c/d = 2$, $r/d = 0.25$ geometry shows a transition to $\partial C_y/\partial\alpha > 0$ at approximately 1° , and this angle will be referred to as the galloping angle. When c/d is increased to 3 for the same corner radius, the galloping angle increases to $\sim 4^\circ$. Interestingly, the geometries with $r/d = 0.5$ show the same galloping angle as that for $r/d = 0.25$ at the same c/d . The angle at which $\partial C_y/\partial\alpha$ transitions back to negative also remains relatively unchanged with r/d . The main difference observed is that for $c/d = 3$, $r/d = 0.5$ there are two closely spaced regions of $\partial C_y/\partial\alpha > 0$. This hard galloping behavior is consistent at $Re_d = 10,000$ for $c/d = 2$, although for $c/d = 3$ the galloping angle is reduced for $r/d = 0.5$ compared with 0.25 . These results demonstrate that for Re_d and r/d cases where hard galloping is observed, the galloping angle is mainly governed by c/d . This is in exception to $c/d = 3$ at $Re_d = 10,000$. The galloping angle is related to the susceptibility to hard galloping, since a larger galloping angle is equivalent to a larger initial disturbance that would be required for an elastically mounted body to reach that value of α instantaneously. Since the galloping angle tends to increase with side ratio, this leads to a decrease in the susceptibility to hard galloping.

4. Conclusions

This experimental study investigates the effects of side ratio, c/d , and corner radius, r/d , on the galloping behavior of rectangular cylinders at Reynolds numbers between 1000 and $10,000$. Three different c/d values are considered, 1 , 2 , and 3 , along with three different corner radii: $r/d = 0$, 0.25 and 0.5 . Lift and drag forces are measured for varying angles-of-attack and Reynolds number, and from this the normal force coefficient is computed. The variation in C_y (the force coefficient in the galloping direction) with angle-of-attack is used to assess the galloping behavior of each geometry. In addition to this, surface pressure distributions are presented for $c/d = 1$, $r/d = 0$ and 0.25 , and $c/d = 3$, $r/d = 0$.

In general, the results demonstrate that the transverse galloping behavior is Reynolds number dependent over the investigated range. This is particularly true for several geometries, where there is a distinct change in behavior between the "low" Reynolds number range, defined as $Re_d \leq 2500$, and the "high" Reynolds number range, $Re_d \geq 5000$. This is an important result, as the majority of experimental galloping studies in literature focus on Reynolds numbers of $\mathcal{O}(10^4)$ and larger. New contributions from this study include results for $10^3 \leq Re_d \leq 10^4$ and the effect of corner radius for varying side ratio.

In the high Reynolds number regime, the results demonstrate that the sharp-cornered cylinders with side ratio 1 and 2 are unstable with respect to galloping, which is consistent with literature for $Re_d \geq 10^4$. It is known that as c/d increases, $r/d = 0$ rectangular cylinders become stable, and this transition to stability is reached in this study at $c/d = 3$. Increasing the corner radius is found to have a stabilizing effect in that it can cause a decrease in the magnitude of a positive C_y slope, or a transition from positive to negative C_y slope and therefore, a body that is stable. A similar stabilizing effect is observed by increasing c/d , with the exception of $r/d = 0$ where both $c/d = 1$ and 2 are approximately equally unstable.

Several interesting behaviors are observed in the low Reynolds number range. The sharp-cornered $c/d = 3$ geometry is unstable, which is opposite to the behavior at high Reynolds number. Furthermore, increasing c/d has a destabilizing effect for $r/d = 0$, which again is opposite to the high Reynolds number behavior. The effect of increasing r/d for both low and high Reynolds number is generally stabilizing for $c/d = 1$ and 3 . For $c/d = 2$, the corner radius effect is non-monotonic

and shows different behavior for $Re_d = 1100$ and 2500 . Detailed characterization of the boundary layer behavior in this low Reynolds number range is required to understand the flow physics that leads to this type of non-monotonic behavior.

Surface pressure distributions are used to gain insight into the nature of the flow as it relates to galloping stability. For $c/d = 1$, $r/d = 0$, which is unstable, the increase in C_y with increasing α near $\alpha = 0^\circ$ is related to the flow on the upper and lower faces of the cylinder remaining separated. Once the flow reattaches on the bottom face, a maximum in C_y occurs and the slope with α becomes negative. This is similarly observed for $c/d = 1$, $r/d = 0.25$ where the formation of a larger region of attached flow on the bottom half of the cylinder coincides with a maximum in C_y . Unlike $c/d = 1$, the flow on the upper and lower surfaces for $c/d = 3$, $r/d = 0$ separates but reattaches at $\alpha = 0^\circ$. A small increase in α above 0° causes a shrinking in the length of the separated zone on the bottom face for high Reynolds number, while for low Reynolds number the flow on the bottom face is relatively unchanged; these cases are stable and unstable, respectively. Thus, a general observation is made that stability with respect to galloping occurs when the length of the separation zone on the bottom half of the cylinder decreases with increasing angle-of-attack. Conversely, when such a decrease does not take place, and the pressure on the top face increases with angle-of-attack, instability to galloping is observed. It is not clear if the shrinking of the mean separation zone on the bottom surface and the change of the separation zone pressure on the top face are inter-linked. Direct measurement of the boundary layer characteristics are required to confirm the flow behavior inferred from the present pressure data.

The final aspect of this study concerns the susceptibility of geometries that are stable to becoming unstable as hard oscillators, known as hard galloping. This effect is observed for $c/d = 2$ and 3 , in particular for $r/d = 0.25$ and 0.5 . The results demonstrate that side ratio has a dominating effect on hard galloping, as the galloping angle for a particular c/d is generally unchanged with r/d . Increasing the side ratio from 2 to 3 increases the galloping angle, and thus makes the body less susceptible to hard galloping.

Declaration of competing interest

The authors declare that they have no known competing financial interests or personal relationships that could have appeared to influence the work reported in this paper.

Acknowledgments

This project is funded through ARO, USA grant number W911NF1710153. The views and conclusions contained in this document are those of the authors and should not be interpreted as representing the official policies, either expressed or implied, of ARO or the U.S. Government. The U.S. Government is authorized to reproduce and distribute reprints for Government purposes notwithstanding any copyright notation herein.

References

- Bearman, P., Gartshore, I., Maull, D., Parkinson, G., 1987. Experiments on flow-induced vibration of a square-section cylinder. *J. Fluids Struct.* 1 (1), 19–34.
- Bearman, P., Luo, S., 1988. Investigation of the aerodynamic instability of a square-section cylinder by forced oscillation. *J. Fluids Struct.* 2 (2), 161–176.
- Bergeron, K., Ecklebe, D., McClure, K., Johari, H., Curlett, T., Pitman, B., 2009. Parachute suspension line drag analysis. In: 20th AIAA Aerodynamic Decelerator Systems Technology Conference and Seminar. pp. 2009–2982.
- Blevins, R.D., 2001. *Flow-Induced Vibration*, second ed. Krieger Publishing Company.
- Carassale, L., Freda, A., Marrè-Brunenghi, M., 2014. Experimental investigation on the aerodynamic behavior of square cylinders with rounded corners. *J. Fluids Struct.* 44, 195–204.
- Feero, M., Naguib, A.M., Koochesfahani, M.M., 2019a. Geometry effects on the galloping instability of rectangular cylinders at low Reynolds number. In: AIAA Scitech 2019 Forum. 2019–1340.
- Feero, M.A., Naguib, A.M., Koochesfahani, M.M., 2019b. Single-component force balance for the measurement of low-magnitude mean aerodynamic loads. *Meas. Sci. Technol.* 30 (11), 115301.
- Huang, R., Lin, B., Yen, S., 2010. Time-averaged topological flow patterns and their influence on vortex shedding of a square cylinder in crossflow at incidence. *J. Fluids Struct.* 26 (3), 406–429.
- Le, H., Moin, P., Kim, J., 1997. Direct numerical simulation of turbulent flow over a backward-facing step. *J. Fluid Mech.* 330, 349–374.
- Luo, S., Yazdani, M.G., Chew, Y., Lee, T., 1994. Effects of incidence and afterbody shape on flow past bluff cylinders. *J. Wind Eng. Ind. Aerodyn.* 53 (3), 375–399.
- Mannini, C., Marra, A., Bartoli, G., 2014. VIV-galloping instability of rectangular cylinders: Review and new experiments. *J. Wind Eng. Ind. Aerodyn.* 132, 109–124.
- Massai, T., Zhao, J., Jacono, D.L., Bartoli, G., Sheridan, J., 2018. The effect of angle of attack on flow-induced vibration of low-side-ratio rectangular cylinders. *J. Fluids Struct.* 82, 375–393.
- Naudascher, E., Rockwell, D., 2005. *Flow-Induced Vibrations: An Engineering Guide*. Dover Publications.
- Noda, H., Nakayama, A., 2003. Free-stream turbulence effects on the instantaneous pressure and forces on cylinders of rectangular cross section. *Exp. Fluids* 34 (3), 332–344.
- Norberg, C., 1993. Flow around rectangular cylinders: pressure forces and wake frequencies. *J. Wind Eng. Ind. Aerodyn.* 49 (1–3), 187–196.
- Parkinson, G., Brooks, N., 1961. On the aeroelastic instability of bluff cylinders. *J. Appl. Mech.* 28 (2), 252–258.
- Parkinson, G., Smith, J., 1964. The square prism as an aeroelastic non-linear oscillator. *Quart. J. Mech. Appl. Math.* 17 (2), 225–239.
- Piccardo, G., Carassale, L., Freda, A., 2011. Critical conditions of galloping for inclined square cylinders. *J. Wind Eng. Ind. Aerodyn.* 99 (6–7), 748–756.
- Siefers, T., Greene, K., McLaughlin, T., Bergeron, K., 2013. Wind and water tunnel measurements of parachute suspension line. In: 51st AIAA Aerospace Sciences Meeting Including the New Horizons Forum and Aerospace Exposition. 2013–0064.

- Siefers, T.M., McLaughlin, T.E., Bergeron, K., 2014. Wind tunnel characterization of fluid-structure interactions for various suspension lines. In: 44th AIAA Fluid Dynamics Conference. pp. 2014–2771.
- White, F.M., 1974. *Viscous Fluid Flow*. McGraw-Hill, pp. 172–178 (Ch. 3).
- Yarusevych, S., Sullivan, P.E., Kawall, J.G., 2006. Coherent structures in an airfoil boundary layer and wake at low Reynolds numbers. *Phys. Fluids* 18 (4), 044101.